Nanoparticle Films and Photonic Crystal Multilayers from Colloidally Stable, Size-Controllable Zinc and Iron Oxide Nanoparticles

Engelbert Redel, Peter Mirtchev, Chen Huai, Srebri Petrov, and Geoffrey A. Ozin*

Materials Chemistry and Nanochemistry Research Group, Center for Inorganic and Polymeric Nanomaterials, Chemistry Department, 80 St.George Street, University of Toronto, Toronto, M5S 3H6, Ontario, Canada

ABSTRACT We report a facile sol−gel synthesis of colloidally stable Fe_2O_3 and ZnO nanoparticles in alcoholic solvents, ROH, where R = methyl, ethyl, *n*-propyl, isopropyl, and *tert*-butyl. We show that nanoparticles of ZnO (4−42) nm and Fe_2O_3 (4−38 nm) monotonically increase in size upon increasing the alkyl chain length and branching of the alcohol solvent. These colloidally stable and size-controllable metal oxide nanoparticles enable the formation of high optical quality films and photonic crystal multilayers whose component layer thickness, refractive index, porosity, and surface area are found to scale with the nature of the alcohol. Utility of these colloidally stable nanoparticles is demonstrated by preparation of one-dimensional porous photonic crystals comprising ncZnO/ncWO$_3$ and ncFe_2O_3/ncWO$_3$ multilayers whose photonic stop band can be tuned by tailoring nanoparticle size. Myriad applications can be envisaged for these nanoparticle films in, for example, heterogeneous catalysis, photocatalysis, electrocatalysis, chemical sensors, and solar cells.

KEYWORDS: Fe_2O_3 · ZnO · metal oxide nanoparticles · size tunability · porous films · multilayer Bragg mirrors

Transition metal oxide nanomaterials are attractive for applications in catalysis, sensing, energy storage and conversion, optics, and electronics.[1−5] Therefore, simple, robust, widely applicable and cost-effective synthesis procedures are required for tailoring the size, shape, and crystallinity of nanoparticle metal oxide materials. Typically there exist two major approaches[6,7] for achieving this goal: surfactant-directed and solvent-controlled methods.[8] The ability of a surfactant to mediate the growth and cap the surface of nanoparticles provides advantages such as shape control, colloidal stability, and surface functionality. In turn, this enables the surface properties and solubility in a variety of solvents to be tailored as desired. The surfactant route also permits impressive control over the monodispersity of metal oxide nanoparticles.[9] Solvent-based approaches offer an alternative to surfactants by allowing common organic solvents to act as a reactant and the nucleation and growth medium, allowing high-purity nanomaterials to be synthesized in surfactant-free environments. These solvent-based approaches are robust and widely applicable, because the synthesis mixture consists of only two components, metal oxide precursor and solvent. This results in high purity products reducing the need for purification steps and simplifying characterization. The use of solvent-controlled syntheses[10] for metal oxide nanoparticle production also yields materials with highly accessible surfaces, which is crucial for applications in gas sensing[11] and heterogeneous catalysis.[12] The ability to correlate synthesis conditions with metal oxide nanoparticle size, morphology, and optical properties is still lacking in the literature today. This paper is an attempt to remedy the situation.

Herein we present details of the alcohol mediated, size-controllable synthesis of two archetypical, colloidally stable metal oxide nanoparticle systems, ZnO and Fe_2O_3. We study the effect of the alcohol solvent/reactant on the optical properties of thin films made from these nanoparticles. Presented also is an optical application, involving the preparation of porous one-dimensional photonic crystals, called Bragg mirrors (BMs) with a tunable photonic stop band position based on nanoparticle size. The approach presented herein allows tuning of the properties of metal oxide nanoparticle dispersions and films, including thickness, refractive index, porosity, and surface area, based solely on the nature of the alcohol solvent used in the synthesis.

ZnO and Fe_2O_3 nanoparticles were synthesized in various alcohol solvents or

* Address correspondence to gozin@chem.utoronto.ca.

Received for review December 14, 2010 and accepted March 10, 2011.

Published online March 10, 2011
10.1021/nn103464r

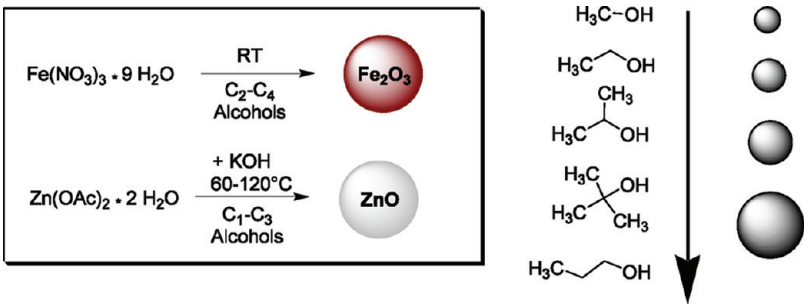

Scheme 1. Schematic illustration of the synthesis of nanoparticle metal oxides in alcohol solvents showing solvent dependent size effects.

TABLE 1. Observed Metal Oxide Nanoparticle Size (nm) from STEM and PXRD, Surface Area BET and Used Alcoholic Reaction Solvent in the Synthesis

metal oxide nanoparticle	solvent or solvent mixture	size (nm) (STEM)[a]	size (nm) (XRPD)[b]	BET (m^2/g) [c]
ZnO	methanol	3–5	3.9 ± 0.4	151
ZnO	ethanol	6–12	10 ± 1.7	98
ZnO	isopropyl alcohol	17–45	42 ± 8.6	30
(Fe_2O_3)	methanol/H_2O			
α-Fe_2O_3	ethanol/H_2O	4–7	4.6 ± 0.4[d]	242
			7.1 ± 1.2[e]	
α-Fe_2O_3	isopropyl alcohol/H_2O	10–22	17.6 ± 3	192
Fe_2O_3	*tert*-butyl alcohol/H_2O	12–25	17.9 ± 6[d]	116
			19.3 ± 9[f]	
Fe_2O_3	*n*-propyl alcohol/H_2O	15–47	37.4 ± 9[d]	56
			19.3 ± 6[f]	

[a] STEM images were obtained using a Hitachi HD-2000 in the Z-contrast mode at an accelerating voltage of 200 kV and an emission current of 30–50 μA. [b] The crystal phase and particle size was analyzed by powder X-ray diffraction (PXRD). The Rietveld refinement was carried out with Bruker AXS general profile fitting software Topas. [c] Physisorption measurements of 40 point adsorption/desorption isotherms, multipoint (5 points) BET methods were used to determine the surface area (m^2/g). [d] Hematite phase. [e] Goethite phase. [f] Maghemite phase.

water/alcohol mixtures from commercially available sources $Zn(OAc)_2 \cdot 2H_2O$ and $Fe(NO_3)_3 \cdot 9H_2O$ at room temperature for Fe_2O_3 and 60–120 °C for ZnO, as shown in Scheme 1. Sol–gel processes usually include a solution phase precursor, which undergoes various hydrolysis and polycondensation reactions to yield an interconnected metal oxide network. In sol–gel[13] metal oxide syntheses, the formation of M–O–M bridges generally represents the first step of the nucleation process followed by further condensation steps and growth into an extended network to form the final nanocrystal structure. A slow and controlled progression of the hydrolysis–condensation steps thereby ensures a high crystallinity of the desired metal oxide material. Colloidal stabilization in surfactant-free synthesis processes is based on the presence of electrical double layer repulsive charges on the nanoparticle surface, originating from ionization of surface groups or adsorption of charged species present in the reaction medium.[14–16] Furthermore, the alcohol oxygen basicity and the steric demands of the alkyl group of the alcohol will influence the growth of the nanoparticles. To observe the effect of the solvent on the growth of the nanoparticle, the concentration of metal precursor was kept constant while varying the nature of the alcoholic reaction medium.

ZnO nanoparticles were formed in MeOH, EtOH, and *i*-PrOH from $Zn(OAc)_2 \cdot 2H_2O$ and precipitated with alcoholic KOH solution. The oxygen of the metal oxide is likely provided by the Zn(II) hydroxide intermediates in the synthesis mixture formed *via* alcoholysis of the precursor.[17,18] In the case of ZnO, Table 1 and Figure 3a demonstrates the approximately linear trend observed between the nanoparticle size and the alkyl chain length of the alcohol employed in the synthesis. The size of the ZnO nanoparticles increases in the order of *i*-PrOH > EtOH > MeOH. Powder X-ray diffraction (PXRD) of the ZnO nanoparticles showed pure Wurtzite phase, (see Supporting Information Figures S1–S3). The ZnO nanoparticle sizes were obtained by PXRD *via* Rietveld refinement and electron microscopy techniques, with good agreement obtained between the two methods, see Table 1. The size increase is observed by the diagnostic red-shifting of the photoluminescence (PL) maximum of the ZnO nanoparticles arising from quantum size effects, Figure 1a. Additional optical absorption measurements showing the quantum size induced red shift, as well further STEM images and bright field/HR-TEM images, are incorporated in the

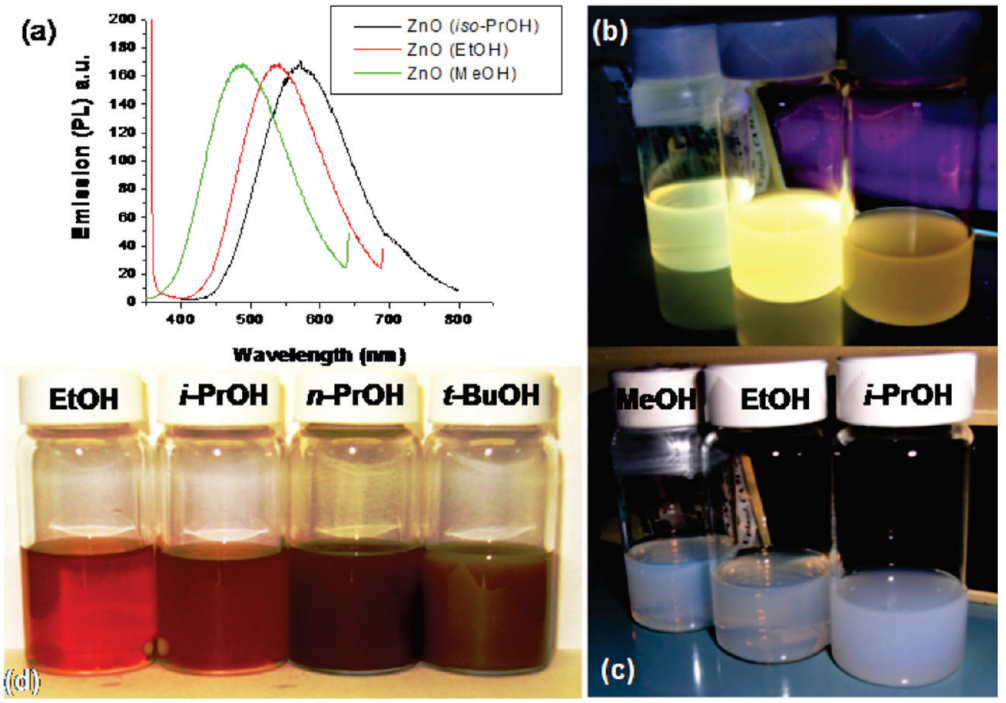

Figure 1. (a) PL spectra (UV-excitation) of different sized ZnO NPs samples prepared in various alcoholic solvents (MeOH, EtOH, *i*-PrOH). (b) Photograph showing visible wavelength photoluminescence of ZnO dispersions synthesized in MeOH (green), EtOH(yellow), and *i*-PrOH (orange/red) under UV-excitation. (c) Photograph of ZnO dispersions in MeOH, EtOH, and *i*-PrOH. (d) Photograph of Fe_2O_3 dispersions synthesized in different ROH/water (4:1) mixtures, R = EtOH, *n*-PrOH, *i*-PrOH, and *t*-BuOH.

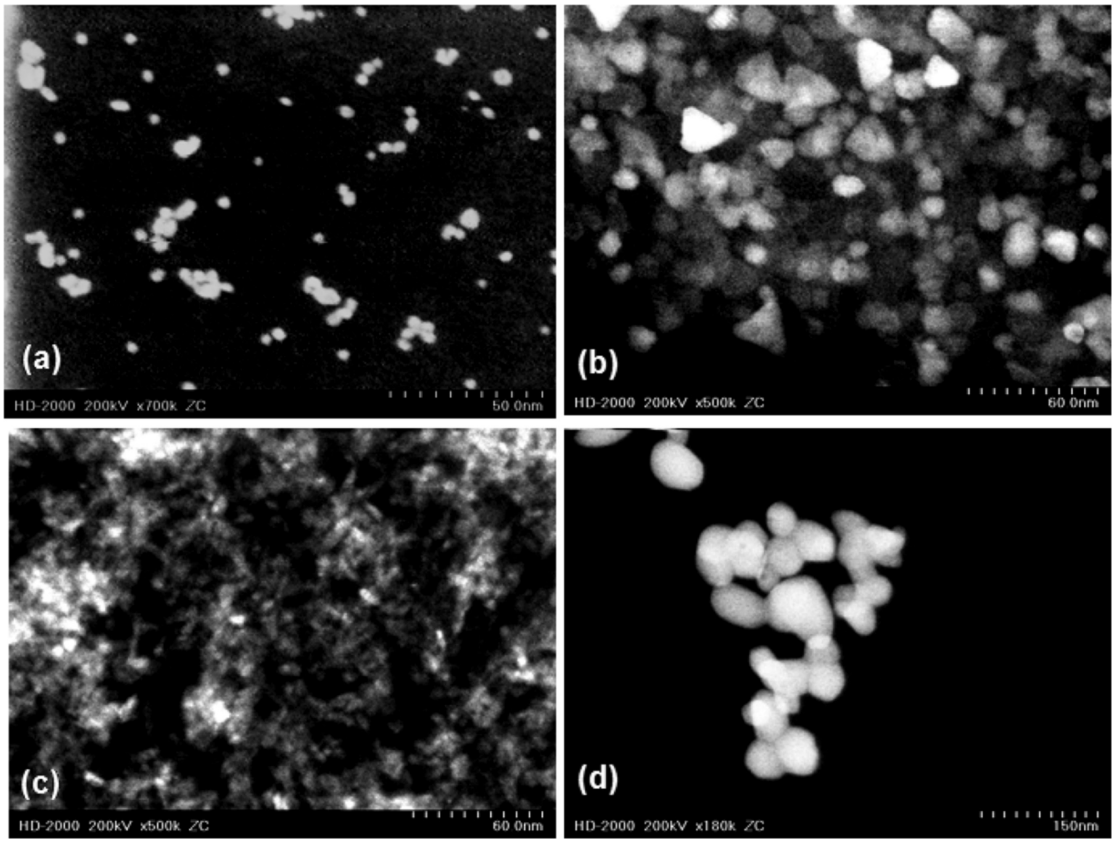

Figure 2. (a) STEM image of ZnO NPs from MeOH dispersion; (b) STEM image of ZnO NPs from *i*-PrOH dispersion; (c) STEM image of Fe_2O_3 NPs from EtOH/water dispersion; (d) STEM image of Fe_2O_3 NPs from *n*-PrOH/water dispersion.

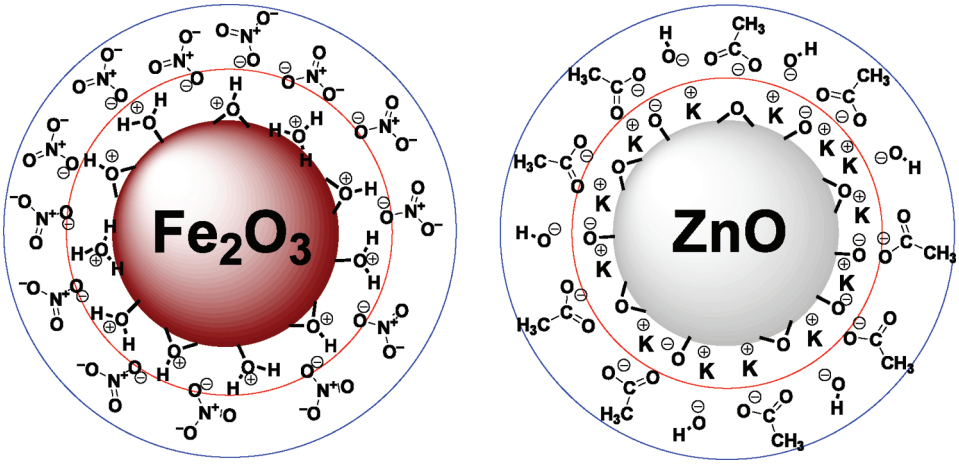

Scheme 2. Schematic illustration of the surface charge stabilization responsible for colloidal stability of Fe_2O_3 and ZnO nanoparticles, with a red inner Stern Layer and a blue diffuse counter anion layer.

supporting material (see Supporting Information Figures S22 and S28). The larger and less monodisperse ZnO nanoparticles synthesized in *i*-PrOH scatter more light and result in more turbid dispersions, in comparison to the almost transparent ZnO dispersions synthesized in MeOH, Figure 1b,c. STEM images are provided in Figure 2 panels a and b, demonstrating the spherical morphology of the synthesized ZnO nanoparticles. Zeta potential measurements,[19] (Supporting Information Figure S16−S19) of a dilute (10:1, H_2O:EtOH) ZnO/EtOH dispersion at pH = 7.16 showed a positive zeta potential ζ of 31.5 $\pm$ 0.4 mV consistent with a negatively charged ZnO nanoparticle surface surrounded by K^+ counterions in the Stern Layer (Scheme 2). Further colloidal stability measurements were done at a variety of pH values (12.6−1.9), and the isoelectric point of the dispersion was estimated at pH 9.4 as the point where the zeta potential is equal to zero (see Supporting Information Figure S20). The presence of the potassium shell was confirmed by energy dispersive X-ray spectroscopy (see Supporting Information Figure S23).

Fe_2O_3 nanoparticles are of great interest because of their magnetic,[20] photocatalytic,[21] and photoelectrochemical applications.[22,23] Fe_2O_3 nanoparticles were synthesized at room temperature in alcohol/H_2O mixtures (4:1) from $Fe(NO_3)_3 \cdot 9H_2O$ and the subsequent addition of H_2O, which initiates the polycondensation reactions and provides an oxygen source for the growth of metal oxide nanoparticles. No Fe_2O_3 NPs were observed when the reaction was conducted in methanol, the PXRD analysis showing only the presence of $Fe_4NO_3(OH)_{11}$ species, which convert to pure α-hematite upon calcination at 600 °C, (see Supporting Information Figures S4 and S9). By using ethanol as the reaction solvent, we obtained a mixture of α-hematite and goethite phases, which were converted to pure α-hematite after calcination at 600 °C (Supporting Information Figures S5 and S10). Interestingly, with *i*-PrOH as the solvent, pure α-hematite was formed without the need for calcination; *n*-PrOH and *t*-BuOH led to mixed phases of α-hematite and maghemite, (see Table 1 and Supporting Information Figures S6−S8). STEM images in Figures 2c and 2d show the spherical morphology exhibited by the prepared nanoparticles in every solvent. Additional optical absorption measurements as well as further STEM images and bright field/HR-TEM are shown in the Supporting Information Figures S21 and S30. The Fe_2O_3 nanoparticle size was found to scale in the order of *n*-PrOH > *t*-BuOH > *i*-PrOH > EtOH as shown in Table 1 and Figure 3a,b. This trend parallels the observed particle size behavior in the ZnO system with the exception that the largest particles are obtained in *n*-PrOH. The nanoparticle sizes as a function of the reaction solvent are shown in Table 1, and an photograph of the various dispersions is presented in Figure 1d. Zeta potential measurements,[17] (see Supporting Information Figures S17 and S19), of a dilute (10:1, H_2O:EtOH) Fe_2O_3/EtOH dispersion at pH = 2.26 showed a strong positive ζ of 20.1 $\pm$ 1.1 mV consistent with a shell of protonated alkoxides in the Stern layer. Further colloidal stability measurements were done at a variety of pH values (2.3−11.8), and the isoelectric point was estimated at pH 7.7, at a zeta potential of 0 (see Supporting Information, Figure S19).

Nucleation and Growth Model. The synthesis of ZnO and Fe_2O_3 nanoparticles in alcohol solvents are considered to be sol−gel in nature, involving, respectively, base and acid catalyzed hydrolytic polycondensation reactions of the type M−OH/OR + HO−M → M−O−M.[24] Growth of so-formed seeds creates nanoparticles with surface OH groups. It is expected that the rates of the initial hydrolytic polycondensation reactions will play a role in the formation of embryonic seeds responsible for the nucleation and growth of the nanoparticles. The faster these reactions are, the larger will be the initial burst of seeds that can grow to smaller nanoparticles. By analogy with the well-studied Stöber

TABLE 2. Film Thickness (nm), Refractive Index (RI), Specific Porosity, and Pore Volume and Pore Size Distribution Listed According to the Used Alcoholic Synthesis Solvent

metal oxide NPs	solvent or solvent mixture	film thickness SE (nm)[a]	film thickness SEM (nm)[b]	elipsometric refractive index n (λ_{633} nm)[a]	specific porosity[c] (cc/g)	dV (pore size) [c] (nm)
ZnO	methanol	66 ± 0.2	~57	1.32	0.304	3.7 ± 0.7
ZnO	ethanol	85 ± 0.3	~79	1.29	0.102	6.3 ± 1.7
ZnO	isopropyl alcohol	142 ± 1.5	~150	1.25	0.148	9.2 ± 4.3
α-Fe_2O_3	methanol/H_2O	49 ± 0.2	~46	1.46	0.151	3.9 ± 0.6
α-Fe_2O_3	ethanol/H_2O	60 ± 0.2	~62	1.34	0.223	5.5 ± 2.7
α-Fe_2O_3	isoporpyl alcohol/H_2O	72 ± 0.3	~70	1.25	0.141	7.8 ± 4.7
Fe_2O_3	*n*-propyl alcohol/H_2O	85 ± 0.3	~82	1.20	0.406	38 ± 17
Fe_2O_3	*tert*-butyl alcohol/H_2O	93 ± 0.5	~105	1.16	0.306	32 ± 12
						6.3 ± 1.4

[a] Spectroscopic ellipsometry (SE) analyses were performed at a fixed incidence angle of 75.0° on silicon wafers for porous metal oxide thin films, in the range 1.2−4 eV. Modeling and regression (R^2 = 0.9548−0.9987) of the ellipsometric spectra were performed using Winelli software, refractive index values were measured at λ = 633 nm. [b] SEM images were obtained using a Hitachi S-5200 operating at 1−5 kV for films on silicon substrates. [c] Physisorption measurements of 40 point adsorption/desorption isotherms were performed using N_2 gas (99.9995% purity). Specific porosity, total pore volume, and average pore size were determined through BJH methods by using the Autosorb software Quantachrome AS1Win, see also Supporting Information Figures S16−S19.

silica sol gel system, homogeneous nucleation and growth occurs under acid- or base-catalyzed conditions. In this scheme the slow hydrolysis of $Si(OR)_4$ builds up to the critical concentration required to form nuclei.[25] The dynamic competition between nucleation and growth is controlled by the hydrolysis step with two limiting models: reaction-limited characterized by a strong size dependence of the growth rate, and diffusion-limited growth with a much weaker size dependence.[22] In the silica system, the hydrolytic poly condensation rates tend to follow the order Si-OMe > Si-OEt > Si-OPr > Si-OBu, with electronic (inductive) and steric arguments associated with the different alkoxide groups invoked to explain this trend.[22,26] Therefore it seems likely that related kinetic factors are contributing to the analogous trend observed for nanoparticle sizes of ZnO and Fe_2O_3 formed in these same alcohol solvents.

Zeta Potential Model. In our alcohol based sol−gel syntheses we observe large positive zeta potentials for ncFe_2O_3 in strongly acidic dispersions (pH 2.2) and nc-ZnO in weakly basic dispersions (pH 7.16). Consider first Fe_2O_3 nanoparticles formed in strongly acidic conditions with nitrate ions present. Here we would expect the surface oxide or hydroxide groups to become protonated to give a positive nanoparticle surface potential with adsorbed hydroxonium (H_3O^+), protonated hydroxyl groups ($-OH_2^+$) and protonated oxygens ($-OH^+-$) in the Stern layer. This simple model can rationalize the positive zeta potential of 20.1 mV (see Scheme 2). In the case of ZnO nanoparticles synthesized under slightly basic conditions with hydroxide and potassium ions present, any surface hydroxides will likely deprotonate to form a negative surface charge on the nanoparticle, which should associate with an excess of (K^+) in the Stern layer thereby making the zeta potential positive at 31.5 mV (see Scheme 2).

Nanoparticle Thin Films. The resulting ZnO and Fe_2O_3 nanoparticle dispersions were filtered, and polyethyleneglycol (PEG), MW = 20.000 (2−10 wt %), was added before spin-coating on Si-wafers. The addition of PEG was employed to improve nanoparticle adhesion to the substrate and ensure good film quality; it undergoes complete carbonization upon calcination at 600 °C. The resulting porous nanoparticle metal oxide thin films, (see Supporting Information Figures S24−S26), and corresponding powder samples were analyzed by spectroscopic ellipsometry (SE), SEM cross-section analysis, and physisorption BET (N_2) measurements (40 absorption/desorption point isotherms) to determine the optical thickness (nm), refractive index RI, (n) surface area (m^2/g), specific porosity (cc/g), pore size, and pore size distribution (nm). A roughly linear correlation was observed between the nanoparticle size and the film thickness, refractive index, and pore-size, caused by the variation of reaction solvent, as shown in Table 2 and Figure 4, (see also Supporting Information Figures S12−S15, S24−S28, and S33−S36). As the nanoparticle size increases, the refractive index (RI) of the resulting thin films decreases from 1.46 to 1.16 for porous Fe_2O_3 thin films and from 1.32 to 1.25 for ZnO thin films accompanied by an increase of the film thickness, for Fe_2O_3 from 46 nm (MeOH) to 93 nm (*tert*-BuOH). The specific porosity (see Supporting Information Figures S12−S15) in cc/g of Fe_2O_3 powder samples increases from ethanol to isopropyl alcohol but decreases in the case of *n*-propyl alcohol and *tert*-butyl alcohol. From nitrogen physisorption measurements on metal-oxide powder samples it was observed that pore sizes increase with increasing particle sizes and particle-size distributions based on the employed alcoholic solvent, see also Table 1. Notably for Fe_2O_3 nanoparticles synthesized in *n*-PrOH and *t*-BuOH a very broad bimodal pore-size distribution was found. This likely arises through a lesser size focusing effect, which

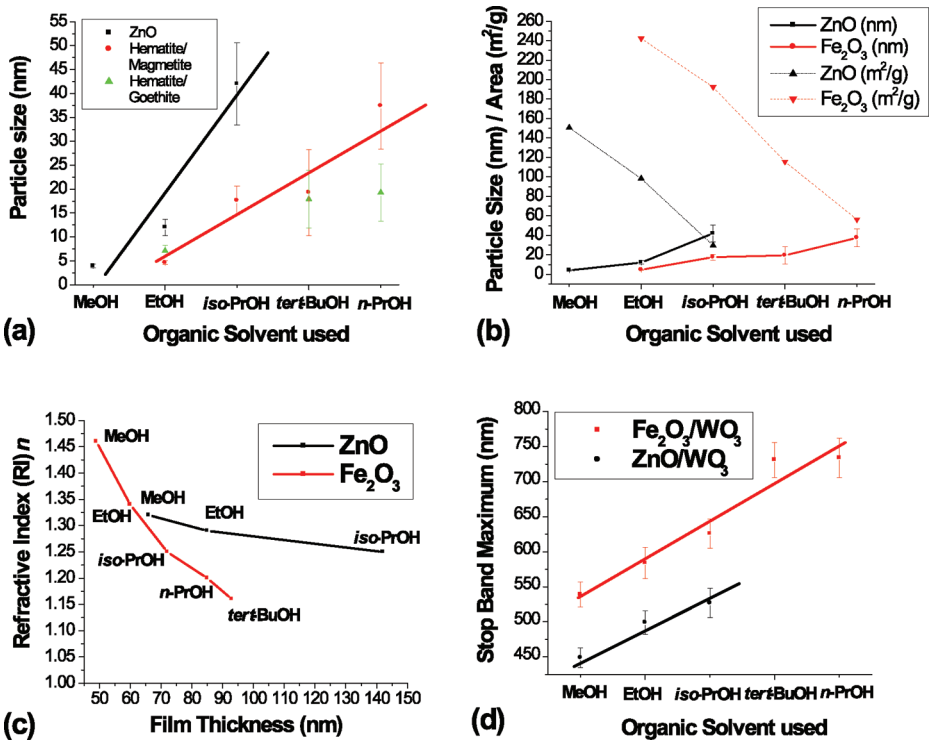

Figure 3. (a) Nanoparticle size as a function of the used alcoholic reaction solvent; (b) nanoparticle size (nm) with error bars, and surface area (m^2/g) as a function of reaction solvent; (c) nanoparticle thin film refractive index as a function of physical film thickness with error bars; (d) nanoparticle Fe_2O_3/WO_3 and ZnO/WO_3 Bragg mirror photonic stop band position with error bars as a function of reaction solvent.

occurs in higher alcohols as well through the formation of two different phases, α-hematite and maghemite from the synthesis process (see Table 2 and Supporting Information Figures S25−S26 and S30−S32). Similar trends with respect to film thickness, porosity, and pore-size distributions were found also for nanoparticle ZnO powders and thin films (see Table 2 and Supporting Information Figures S24 and S27−S29).

Tuning the film thickness, porosity, and the refractive index of Fe_2O_3 and ZnO thin films makes this approach interesting for the design and construction of optical devices such as one-dimensional photonic crystals, BMs, which have found applications in optics as precise wavelength selective mirrors, filters, and sensors.[3,11,27] These BMs consist of alternating layers of high and low dielectric constant materials with constructive interference of reflected light at each interface leading to the formation of a photonic stop gap, a range of energies where the propagation of light is forbidden, analogous to the electrical band gap in semiconductors. The resulting stop band positions of BMs are highly dependent on the thickness, porosity, and refractive index of its constituent layers, and should therefore be expected to vary with increasing particle size based on the nature of the alcohol solvent.

BMs with three double layer, Fe_2O_3/WO_3 and ZnO/WO_3 one-dimensional photonic crystal architectures were prepared by spin coating on silicon wafers and their stop-band positions were measured by optical spectroscopy. WO_3 nanoparticles were employed because of the high refractive index of this material in the visible range, thus improving the interlayer contrast in the BMs which has a dramatic effect on its photonic properties. A red shift for ZnO BMs of 78 nm (from 450 to 528 nm) and for Fe_2O_3 BMs of 195 nm (from 540 to 735 nm) in the stop band position was clearly observed, arising from increased film thickness caused by the presence of larger particles in the iron and zinc oxide layers, while keeping the WO_3 layer at a constant particle size and thickness (see Figure 3d and Figure 4 and Supporting Information Figures S29−S32). Experiments are currently underway to investigate the use of the above Bragg mirrors and single layer thin films as gas sensors based on refractive index and porosity driven changes in the photonic crystal and optical spectra upon adsorption of a variety of analysts.

In conclusion, we report a widely applicable and cost-effective surfactant-free synthesis process for preparing ZnO and Fe_2O_3 metal oxide nanoparticles in different alcoholic solvents ROH with R = Me, Et, *n*-Pr, *i*-Pr, and *t*-Bu. Size tailoring of the synthesized metal oxide nanoparticles was achieved by simply changing the alcohol solvent. This provides a method for the control of nanoparticle thin film properties such as film thickness, refractive index, specific porosity, pore-size distribution, and surface area. Roughly linear correlations were found between these properties and the choice of alcohol reaction solvent. In general, larger

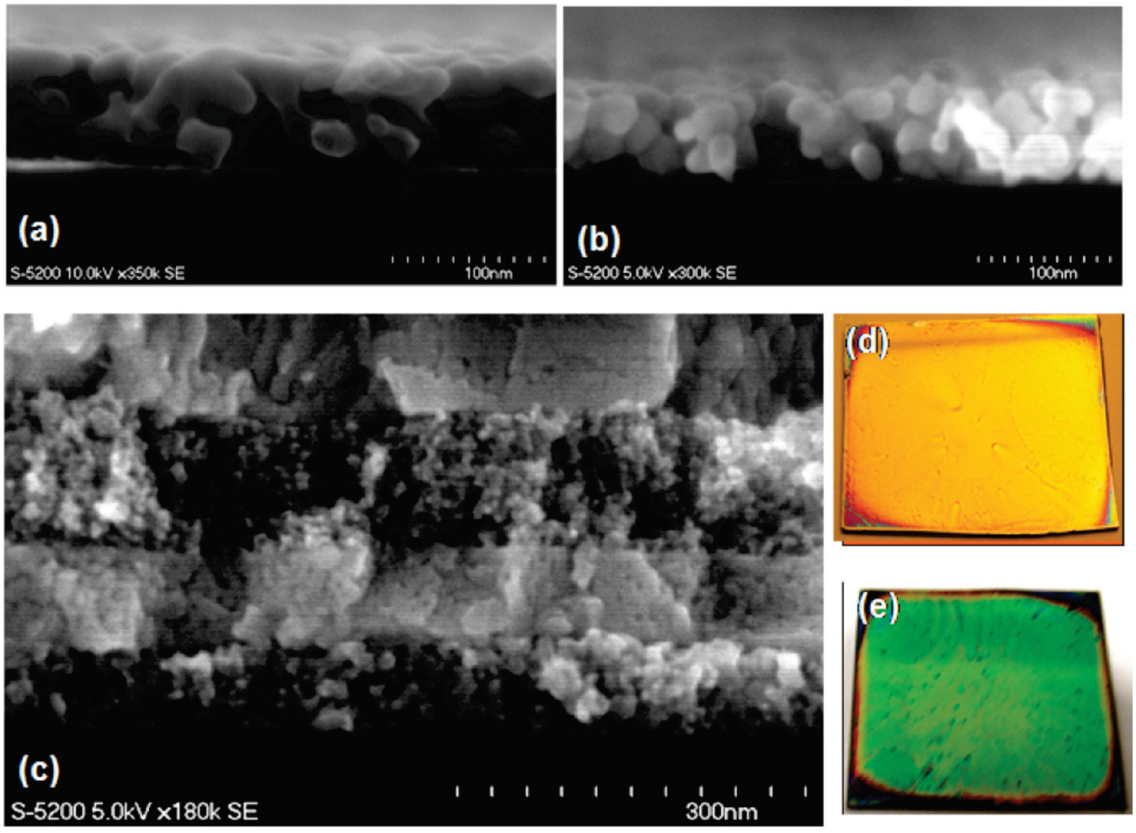

Figure 4. (a) SEM cross section image of a porous nanoparticle α-Fe_2O_3 thin film; (b) SEM cross section image of a porous nanoparticle ZnO thin film; (c) SEM cross section image of two double layers (2DL) of a nanoparticle α-Fe_2O_3/WO_3 BM; (d) optical photograph showing yellow reflectivity of spin-coated 3DL ZnO/WO_3 BM; (e) optical photograph showing green reflectivity of spin coated 3DL nanoparticle α-Fe_2O_3/WO_3 Bragg mirror (BM).

and less monodispersed metal oxide nanoparticles were found with a longer alkyl chain and/or sterically more demanding alkyl group in the order *n*-PrOH > *t*-BuOH > *i*-PrOH > EtOH > MeOH. The resulting Fe_2O_3 and ZnO nanoparticle dispersions were used to make Fe_2O_3/WO_3 and ZnO/WO_3 porous BMs with optical properties that could be tuned with nanoparticle size. By keeping the WO_3 layer porosity and thickness constant, the position of the photonic stop band of the BM was found to monotonically red shift with increasing Fe_2O_3 and ZnO film thickness, originating from the larger nanoparticle sizes in the corresponding solvents. It is anticipated that the method described herein for size tailoring the properties of ZnO and Fe_2O_3 nanoparticles and their thin films properties may be extendable to other metal oxide nanoparticle systems.

METHODS

Materials and Chemicals. $Fe(NO_3)_3 \cdot 9H_2O$ (ACS reagent >98+%), $Zn(OAc)_2 \cdot 2H_2O$ (p.a.), W metal powder (99.9% metal basis), H_2O_2 (30% p.a.), H_2SO_4 (95 to 98 wt%) were obtained from Aldrich and Alfa Aesar. Silicon wafers (University Wafer, Lot, 1-800-216-8346) were obtained from Wafer World.

Experimental Methods. *Synthesis of Fe_2O_3, ZnO, and WO_3 Nanoparticles.* Fe_2O_3 NPs were synthesized by dissolving $Fe(NO_3)_3 \cdot 9H_2O$ (5.05 g, 12.5 mmol) in 80 mL ROH, with *R* = Me, Et, *n*-Pr, *iso*-Pr, or *tert*-Bu, followed by addition of 20 mL deionized water (18.2 μS/cm). The resulting dark-red solution (pH ≈ 1−2) was stirred for 12 h at room temperature (RT). The resulting orange-brown Fe_2O_3 dispersion was stored at RT in air.

ZnO NPs were synthesized according to literature,[28] by dissolving zinc acetate dihydrate $Zn(OAc)_2 \cdot 2H_2O$ (2.95 g, 13.4 mmol) in 125 mL of ROH with R = Me, Et, *iso*-Pr at 60 °C (MeOH), 85 °C (EtOH) or 120 °C (*i*-PrOH). A solution of KOH (Merck, 87%, 1.48 g, 23 mmol) in 65 mL of the corresponding alcohol was added in 10 min to the zinc acetate dihydrate solution under vigorous stirring. Zinc hydroxides precipitated but dissolved again. After 5 min, the solution became translucent and remained so until the nanoparticles started to precipitate after 1.5 h and the solution became turbid; 2 h and 15 min later, the heater and stirrer were removed and the nanoparticles were allowed to precipitate for an additional 2 h. Precipitate and mother liquor were separated, and the precipitate was washed twice with ROH (50 mL). After the washing steps (5 min), the suspension was left unstirred for a minimum of 1 h to reach full precipitation and centrifugated for 5 min at 7300 rpm. The washed and centrifugated precipitate was treated with chloroform (10 mL) to dissolve/disperse the ZnO nanoparticles.

WO_3 NPs were synthesized by dissolution of elemental W powder (mesh 325) 5.53 g (30.1 mol) in 50 mL of H_2O_2 (30% p.a.) at 0 °C by cooling the reaction mixture with an ice-bath. The exothermic dissolution/oxidation process leads to a light-yellow WO_3 dispersion, which was stored in a plastic bottle at 4 °C.

The resulting metal oxide dispersions were filtered through a 0.7 μm Titan 2 HPLC Filter Amber (GMF Membrane) and PEG $[(C_2H_4O)_n \cdot H_2O]$/MW = 20000 was added to the metal oxide nanoparticle dispersion in the range 1−10 wt % before spin-coating. Prior to spin coating the silicon wafers were treated with a mixture of H_2O_2/H_2SO_4 (3:1) (piranha) for at least 1 h and washed with ethanol. The Si wafers were treated under air plasma for at least 5 min to remove impurities and to increase the hydrophilicity of the surface. Spin coating of the films was performed on a Lauriel single wafer spin processor (model WS-400A-6NPP/LITE) at 2500−4000 rpm, 30−60 s. The resulting films were calcined at 600 °C for 15−30 min.

Materials and Methods. Scanning electron microscopy (SEM) images were obtained using a Hitachi S-5200 operating at 1−5 kV for films on silicon substrates, or at 30 kV for films scraped off onto a carbon-coated copper grid. High-resolution scanning transmission electron microscopy (HR-STEM) and EDX spectroscopy were performed on a Hitachi HD-2000 in the Z-contrast mode at an accelerating voltage of 200 kV and an emission current of 30−50 μA. The crystal phase and particle size of the films were analyzed by powder X-ray diffraction (PXRD) using a Siemens D5000 diffractometer and Cu−Kα line as the X-ray source. The Rietveld refinement was carried out with Bruker AXS general profile fitting software Topas.[29] An Autosorb-1 Instrument from Quantachrome™ Instruments (Boynton Beach, Florida, USA) was applied for performing surface area measurement, adsorption/desorption isotherms, pore volume measurement, and pore size distribution analysis. Physisorption measurement of 40 points adsorption/desorption isotherms were measured by N_2 gas (99.9995% purity), multipoint and single point BET methods were used to determine the surface area (m^2/g), mesopore volume, total pore volume, and average pore size were determined through BJH methods. The autosorb software (Quantachrome AS1Win) for data analysis was provided by the manufacturer. Before measuring, powder samples were degassed under vacuum at 200−220 °C for at least ~4 h for drying purposes and for removal of solvent impurities and humidity. Spectroscopic ellipsometry (SE) analyses were performed in a Sopra GES-5E ellipsometer at a fixed incidence angle of 75.0° on silicon wafers, in the range 1.2−4 eV. The modeling and regression of the ellipsometric spectra were performed using the software Winelli provided by the manufacturer. The particle zeta potential for the obtained Fe_2O_3 (Ethanol/H_2O) and ZnO (Ethanol) nanoparticle dispersion was measured through electrophoretic mobility measurements on a ZetaSizer 3000 HSa, Malvern Instruments, Southborough, Boston, MA. A zeta potential transfer standard DTS 1230 (−68 ± 6.8 mV) was tested before measuring the samples. Prior to analysis, the respective metal oxide samples were diluted with deionized H_2O (18.2 μS/cm) in the ratio of 10:1 to obtain optical transparency for the measurements. Particle zeta potential measurements were performed five times for consistency purposes. pH measurements were performed on a VWR SympHony SB70P laboratory pH meter. Optical spectra and micrographs were acquired with an Ocean Optics SD2000 fiber optic spectrophotometer coupled to an optical microscope.

Acknowledgment. G.A.O. is Government of Canada Research Chair in Materials Chemistry and Nanochemistry. Dr. Engelbert Redel thanks the Alexander von Humboldt (AvH) Foundation for a Feodor Lynen Postdoctoral Fellowship; Peter Mirtchev thanks NSERC for a CGSM graduate scholarship.

Supporting Information Available: Figures (S1−S36) contain additional scanning electron and scanning transmission electron microscopy images (SEM-STEM) and SEM-cross sections, powder X-ray diffraction patterns (PXRD) and Rietveld full profile analyses, N_2 physisorption isotherms, BET, poresize distribution analyses, zeta potential measurements, and optical absorption measurements. This material is available free of charge *via* the Internet at http://pubs.acs.org.

REFERENCES AND NOTES

1. Rodriguez, J. A.; Fernandez-Garcia, M. *Synthesis, Properties, and Applications of Oxide Nanomaterials*; Wiley InterScience: New York, 2007; pp 79−119.
2. Niederberger, M.; Antonietti, M. In *Nanomaterials Chemistry: Recent Developments and New Directions*; Rao, N. R. C.; Mueller, A.; Cheetham, A. K., Eds.; Wiley-VCH: Weinheim, Germany, 2007; pp 119−139.
3. Puzzo, D. P.; Bonifacio, L. D.; Oreopoulos, J.; Yip, C. M.; Manners, I.; Ozin, G. A. Color from Colorless Nanomaterials: Bragg Reflectors Made of Nanoparticles. *J. Mater Chem.* **2009,** *19*, 3500–3506.
4. Niederberger, M.; Pinna, N. *Metal Oxide Nanoparticles in Organic Solvents*; Springer-Verlag: London, 2009; pp 53−95.
5. Goesmann, H.; Feldmann, C. Nanoparticulate Functional Materials. *Angew. Chem., Int. Ed.* **2010,** *49*, 1362–1395.
6. Pinna, N.; Neri, G.; Antonietti, M.; Niederberger, M. Nonaqueous Synthesis of Nanocrystalline Semiconducting Metal Oxides for Gas Sensing. *Angew. Chem., Int. Ed.* **2004,** *43*, 4345–4349.
7. Niederberger, M. Nonaqueous Sol−Gel Routes to Metal Oxide Nanoparticles. *Acc. Chem. Res.* **2007,** *40*, 793–800.
8. Pinna, N.; Niederberger, M. Surfactant-Free Nonaqueous Synthesis of Metal Oxide Nanostructures. *Angew. Chem., Int. Ed.* **2008,** *47*, 5292–5304.
9. Park, J.; Joo, J.; Kwon, S. G.; Jang, Y.; Hyeon, T. Synthesis of Monodisperse Spherical Nanocrystals. *Angew. Chem., Int. Ed.* **2007,** *46*, 4630–4660.
10. Jun, Y.-W.; Choi, J.-S.; Cheon, J. Shape Control of Semiconductor and Metal Oxide Nanocrystals through Nonhydrolytic Colloidal Routes. *Angew. Chem., Int. Ed.* **2006,** *45*, 3414–3439.
11. Bonifacio, L. D.; Puzzo, D. P.; Breslav, S.; Willey, B. M.; McGeer, A.; Ozin, G. A. Towards the Photonic Nose: A Novel Platform for Molecule and Bacteria Identification. *Adv. Mater.* **2010,** *22*, 1351–1354.
12. Heiz, U.; Landman, U. *Nanocatalysis*; Springer-Verlag: Berlin, 2008; pp 245−374.
13. Caruso, R. A.; Antonietti, M. Sol−Gel Nanocoating: An Approach to the Preparation of Structured Materials. *Chem. Mater.* **2001,** *13*, 3272–3282.
14. Verway, E. J. W.; Overbeek, J. T., G. *Theory of the Stability of Lyophobic Colloids*; Elsevier: Amsterdam, The Netherlands, 1948; pp 22−65.
15. Garnweiler, G.; Niederberger, M. Organic Chemistry in Inorganic Nanomaterials Synthesis. *J. Mater Chem.* **2008,** *18*, 1171–1182.
16. Niederberger, M.; Garnweiler, G. Organic Reaction Pathways in the Nonaqueous Synthesis of Metal Oxide Nanoparticles. *Chem.—Eur. J.* **2006,** *12*, 7282–7302.
17. Rodriguez-Gattorno, G; Oskam, G. Forced Hydrolysis *vs* Self-Hydrolysis of Zinc Acetate in Ethanol and Isobutanol. *ECS Trans.* **2006,** *3*, 23–28.
18. Ambrozic, G.; Skapin, S.; Majda, O.; Crnjak, Z. The Synthesis of Zinc Oxide Nanoparticles from Zinc Acetylacetonate Hydrate and 1-Butanol or Isobutanol. *J. Colloid Interface Sci.* **2010,** *346*, 317–323.
19. Hunter, R. J. *Zeta Potential in Colloid Science: Principles and Applications*; Academic Press: London, UK, 1988; pp 24−54.
20. Kim, D.; Lee, N.; Park, M.; Kim, B. H.; An, K.; Hyeon, T. Synthesis of Uniform Ferrimagnetic Magnetite Nanocubes. *J. Am. Chem. Soc.* **2009,** *131*, 454–455.
21. Kaneko, M.; Okura, I. *Photocatalysis Science and Technology*; Kodansha & Springer-Verlag: Tokyo, Japan, 2002; pp 69−106.
22. Cesar, I.; Kay, A.; Gonzalez Martinez, J. A.; Grätzel, M. Translucent Thin Film Fe_2O_3 Photoanodes for Efficient Water Splitting by Sunlight: Nanostructure-Directing Effect of Si-Doping. *J. Am. Chem. Soc.* **2006,** *128*, 4582–4583.
23. Satsangi, V. R.; Dass, S.; Shrivastav, R. In *On Solar Hydrogen & Nanotechnology* Vayssieres, L. Ed.; John Wiley & Sons (Asia): Singapore, 2009; pp 349−397.
24. Brinker, C. J.; Scherer, G. W. *Sol-Gel Science: The Physics and Chemistry of Sol-Gel Processing*; Academic Press: London, UK, 1990; pp 97−228.
25. Wang, G.; Li, A.; Zhang, Y. Preparation of Micro-sized Monodisperse Silica Spheres by Hydrolysis of

Tetraethylorthosilicate. *Adv. Mater. Res.* **2010,** *105*−*106*, 466–469.
26. Boukari, H.; Long, G. G.; Harris, M. T. Polydispersity during the Formation and Growth of the Stober Silica Particles from Small Angle X-Ray Scattering Measurements. *J. Colloid Interface Sci.* **2010,** *229*, 129–139.
27. Lotsch, B. V.; Ozin, G. A. Clay Bragg Stack Optical Sensors. *Adv. Mater.* **2008,** *20*, 4079–4084.
28. Pacholski, C.; Kornowski, A.; Weller, H. Self-Assembly of ZnO: From Nanodots to Nanorods. *Angew. Chem., Int. Ed.* **2002,** *41*, 1188–1191.
29. *General Profile and Structure Analysis Software For Powder Diffraction Data, User's Manual*, version 2.1; Topas: Karlsruhe, Germany, 2003.